ues of D_3 at $\pm 0.26\ \mathrm{Cm}^{-2}$. However, since $a_1(t) = a_2(t)$ throughout the domain evolution, the maximum volume fraction of both crystal variants 3 and 4 never exceeds 50%. Consequently, even though the crystal is subjected to the compressive stress $\sigma_3 = -1.78\ \mathrm{MPa}$, the symmetric butterfly loop has a strain change of magnitude 0.545% only, as shown in figure 5.4(b).

Recall that uniform stress and electric field throughout the crystal were assumed in the previous calculation. Now we would like to examine this assumption by using finite element analysis. Again we consider the cases of domain patterns "5354" and "5346", as shown in figures 5.1 and 5.6, subjected to electric field $E_3(t) = E_0 \sin(2\pi t)$ with amplitude $E_0 = 1\mathrm{MVm}^{-1}$ and the applied stress $\sigma_3 = -1.78\ \mathrm{MPa}$. Note that, as in the previous calculations, the domain topology remains unchanged during calculation and that the only factors specifying the domain wall position are a_i. In order to determine U and Ω in equations (5.2) and (5.3) more accurately, a conventional finite element analysis is used to calculate both the elastic displacement field and electric potential in the unit cell. Six-node triangle plane stress elements are used and the yz plane is modelled as both domain patterns studied here are prismatic along the direction of x-axis. Quadratic shape functions are used to describe the displacement and electric field at each point in terms of the nodal displacements, u_i and scalar electric potential ϕ. The same set of material properties as shown in table 5.1 is used for variant 5 and those for other crystal variants are obtained from pure rotation by 90° or 180° according to their orientation.

A typical mesh arrangement and applied boundary conditions are shown in figure 5.8. The displacement of the node at the bottom left of the cube is constrained so that $u_2 = u_3 = 0$. Constraints $u_3 = 0$ and the electrical ground condition $\phi = 0$ are applied on the node at the bottom right. Periodic boundary conditions are applied to every node on the right (R), left (L) surfaces, marked with dashed lines in figure 5.8, and the top (T), bottom (B) surfaces, marked

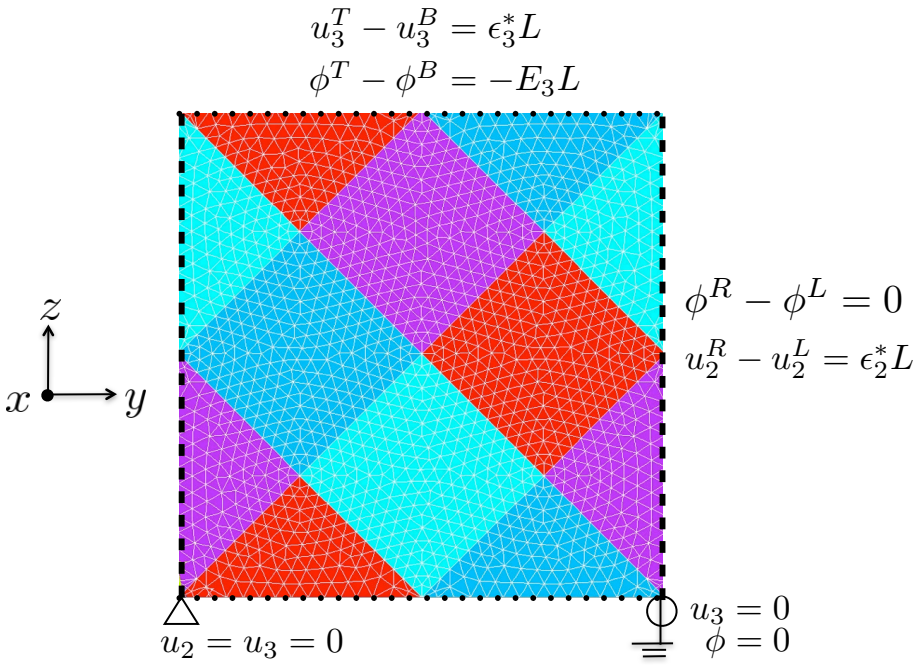

Figure 5.8: The mesh and applied boundary conditions for domain pattern "5346".

with dotted lines in figure 5.8, of the unit cell [7], such that

$$\begin{aligned} u_2^R - u_2^L &= \epsilon_2^* L \\ u_3^T - u_3^B &= \epsilon_3^* L \\ \phi^R - \phi^L &= 0 \\ \phi^T - \phi^B &= -E_3 L \end{aligned} \tag{5.22}$$

where ϵ_p^* is the effective applied average strain which is given in the current configuration by

$$\epsilon_p^* = s_{pq}^* \sigma_q + d_{kp}^* E_k \tag{5.23}$$

Here σ_q and E_k are the applied stress and electric field respectively; s_{pq}^* and d_{kp}^* are the matrices of effective elastic compliance and piezoelectric coefficients. For improved accuracy, s_{pq}^* and d_{kp}^* were determined by the method of Li and Liu [26] (see appendix A). It is worth noting that exact compatibility is not satisfied in the current calculations as stress and electric field are non-uniform due to the material properties varying from domain to domain with respect to

the global co-ordinate system. However, the elastic strain and electric displacement are small compared to the remanent strain and polarization. Thus, this effect can be neglected.

In this way, the assumption of uniform stress and electric field is eliminated. A more accurate Gibbs free energy G can then be obtained. Furthermore, in order to determine $\frac{\partial G}{\partial a_r}$, the rate of Gibbs free energy in respect to the rth domain wall position, $G(a_r + da_r, \boldsymbol{\sigma}, \mathbf{E})$ and $G(a_r - da_r, \boldsymbol{\sigma}, \mathbf{E})$ in equation (5.18) are obtained from two separate finite element calculations which have the same set up but with the position of the nodes on the rth domain wall slightly adjusted to reflect the small change of $\pm da_r$. Here, the values of $\mathrm{d}a$, time step $\mathrm{d}t$ and the initial degrees of freedom a_r are set the same as in the previous calculations. The rate potential, Ψ, is provided by equations (5.16) and (5.21) for the two domain patterns "5354" and "5346". The dielectric and strain hysteresis loops for these domain patterns obtained by finite element analysis are shown using solid lines in figure 5.4(a) and (b), respectively.

In the finite element calculations, the mesh was refined at every time step. The mesh size was set dynamically according to the width of the domains. Such that fine domains are assigned sufficiently small elements. However, whenever $a_r \geq 0.95$ or $a_r \leq 0.05$, domains become too small to mesh easily. Thus the mesh size of these domains is then assigned to match the mesh of nearby domains without further mesh refinement. Figure 5.9 shows the domain evolution for domain pattern "5346". It can be observed that the mesh is refined as the domain pattern evolves.

It is of interest that hysteresis loops generated by accurate calculation of G, using finite element analysis are very similar to those generated using the assumption of uniform stress and electric field, as shown in figure 5.4. The predicted domain pattern evolution generated by the two approaches are also similar. For example, they have identical saturated values of dielectric displacement (D_3) and strain (ϵ_3) in both types of domain patterns. In domain pattern "5346", finite element analysis confirms the result that $a_1(t)$ remains equal to $a_2(t)$ throughout the entire switching procedure, as shown in figure 5.9. However, it can be observed that the

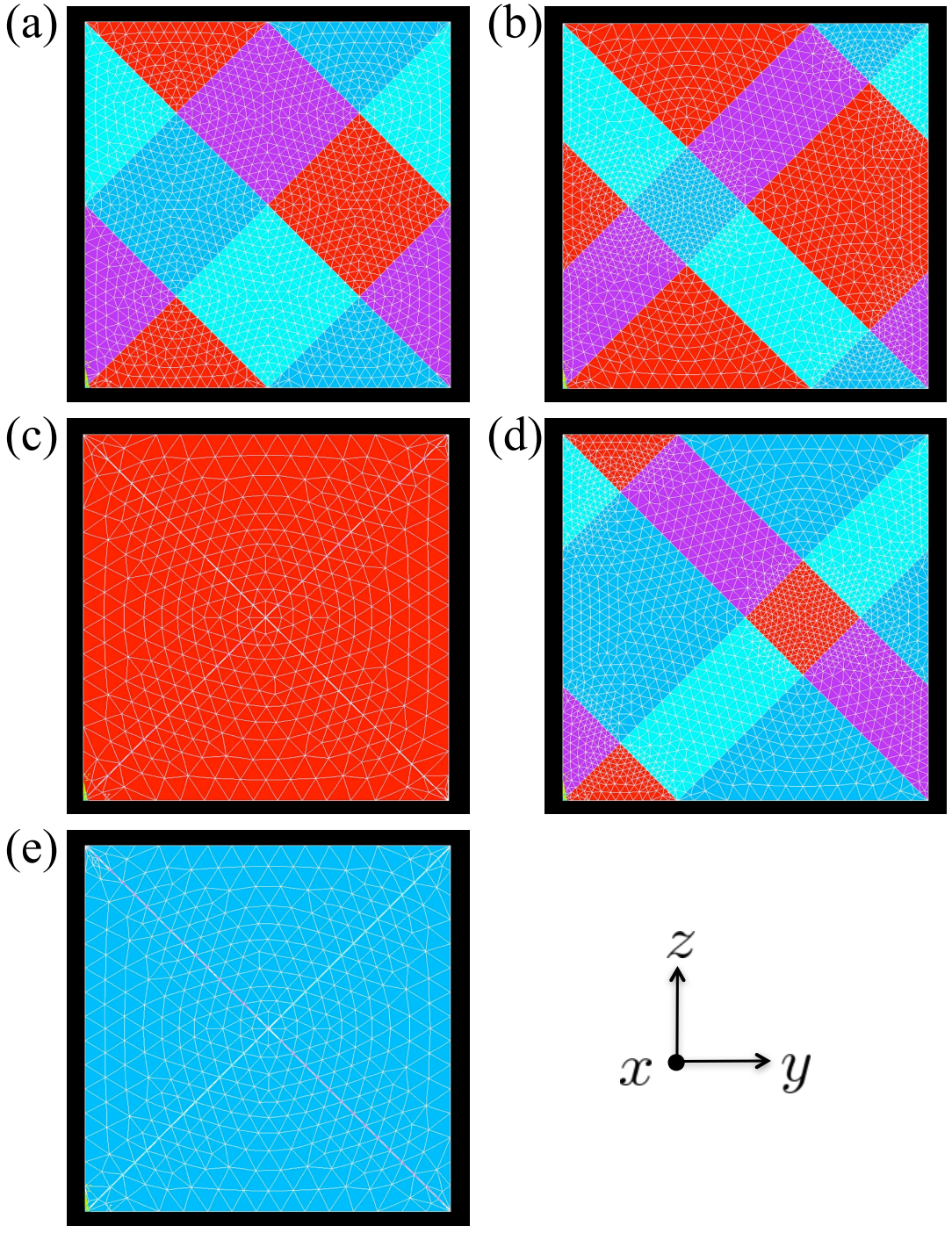

Figure 5.9: The domain evolution for pattern "5346" in the electric loading cycle under stress $\sigma_3 = 1.78\text{MPa}$, predicted by the finite element analysis.

applied compressive stresses have relatively stronger effect on domain switching when uniform stress and electric field are assumed. Figure 5.4(a) shows that in the initial stage of locking of

the domain pattern "5354", the dielectric and strain hysteresis curves decrease firstly and then increase until saturated. Note that the curves generated using the uniform stress and electric field assumption drop deeper than those generated by the finite element analysis indicating that the applied stress induces more 90° domain switching when uniform stress and electric field are assumed. Also, when $E_3 < 0$, the onset of rapid switching is earlier in the Reuss approximation. Such difference in the onset of switching can also be found in the case of domain pattern "5346" shown in figure 5.4(b). Although the assumption of uniform stress and electric field does affect the resulting hysteresis responses slightly, the overall behaviour and many important features of domain switching behaviour can still be well captured. In addition, by using this assumption at domain pattern level, the saving of computation is significant. This issue becomes more crucial in the following studies, as we will consider more than one pattern at every time step to enable the possibility of switching between domain patterns. Therefore, the Reuss assumption is used with reasonable confidence that it does not greatly affect domain evolution in the following section.

5.3 Kinetic model with pivot states

In section 5.2, it is observed that the hysteresis responses are significantly affected by domain arrangement. However, neither of these hysteresis loops shown in figure 5.4 closely resemble the results of the experiment carried out by Burcsu *et al.* [28] on single crystals of $BaTiO_3$, as shown in figure 5.10(c). This suggests that modelling a single domain pattern is not representative of the behaviour of a large ferroelectric single crystal under load. We now explore the possibility of switching between different domain patterns in the sharp interface model.

According to section 3.5.2, there are exactly eight distinct families of rank-2 compatible laminates in the polar tetragonal crystal system: $\{1112\}$, $\{1221\}$, $\{1324\}$, $\{1213\}$, $\{1234\}$, $\{1314\}$, $\{1325\}$, and $\{1342\}$. They are shown in the first row in figure 5.11. Again, the variant

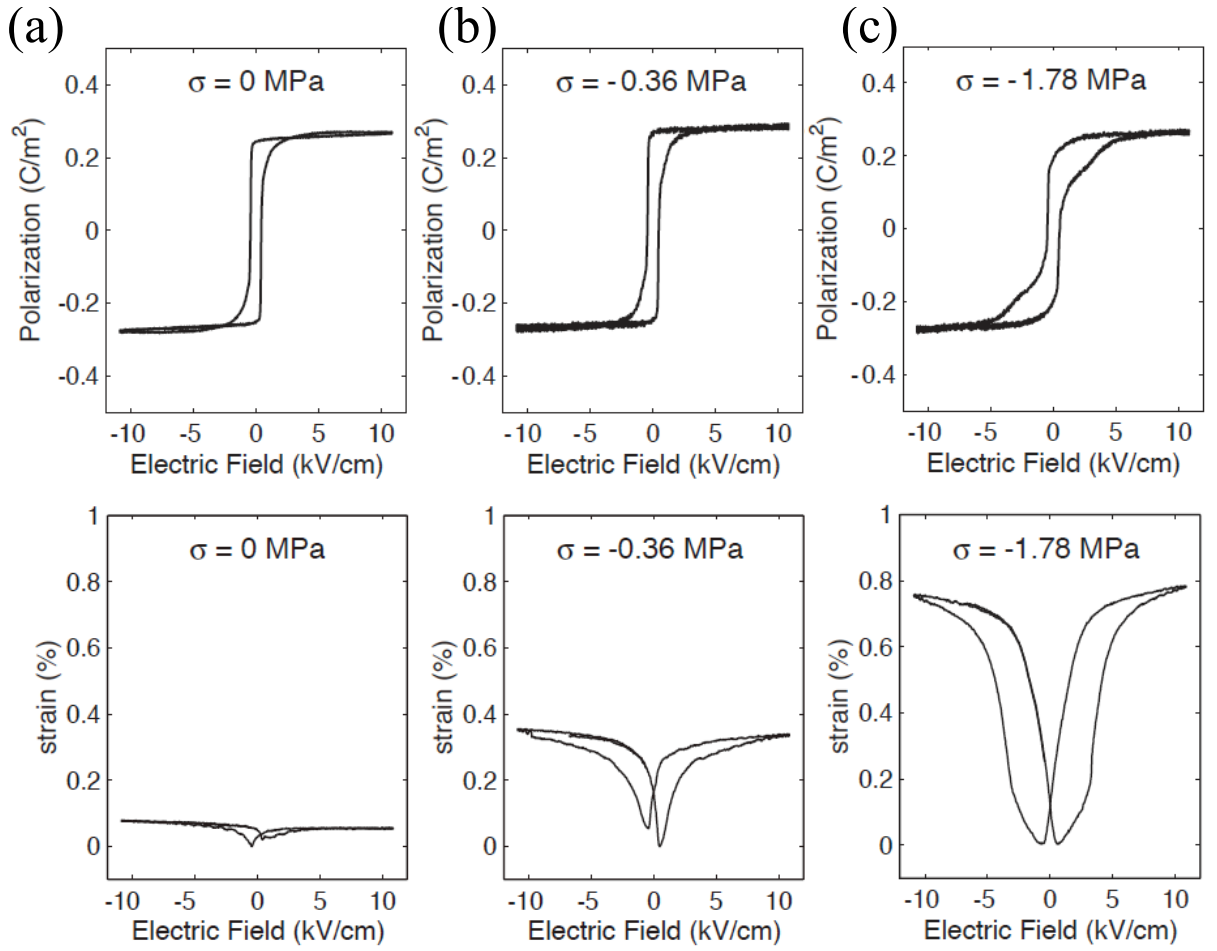

Figure 5.10: Hysteresis responses of single crystal $BaTiO_3$ due to Burcsu *et al.* [28], for a crystal is subjected to a compressive stress $\sigma_3 = 0,\ -0.36$, and -1.78 MPa and a cyclic electric field $E_3 = E_0 \sin(2\pi t) \mathrm{MVm}^{-1}$.

numbers in curly brackets shown in figure 5.11 indicates a family containing all possible domain structures with identical pattern under rotations, reflections and inversions. The domain walls marked with dashed lines in figure 5.11 indicate 180° domain walls which separate domains with anti-parallel polarization directions but with the same remanent strain. Domain walls of this type have no certain habit planes and their normals can lie in any orientation which is perpendicular to the polarization direction of the variants being separated. The flexible orientation of 180° domain walls results in infinite variations of domain arrangements when considering the kinetic formulation. Thus, here we only consider two key orientations of: $[100]$ and $[110]$ 180° domain walls. This limits the number of topologies that must be considered to 12 domain

topologies in the current study as shown in figure 5.12.

Now define a pivot state as a state in which the domain walls of a laminate domain structure reach their extremal position, i.e. the corresponding degree of freedom $a_r \to 1$ or $a_r \to 0$. This reduces a certain domain or set of domains to zero volume and thus the structure jumps to a lower rank. For example, the patterns $\{1314\}$ and $\{1342\}$ can both form limiting states of rank-0 domain pattern $\{1\}$ (see figure 5.11). Thus $\{1314\}$ can reach the pivot state $\{1\}$ and then $\{1314\}$ can nucleate continuously from such a pivot state. However, note that some structures can only alter a_1 domain walls because the a_2 domain walls are sessile until a pivot state is reached, such as domain patterns "1213", "1314", "1325" etc. Equation (5.9) can be used to check if the domain walls are sessile. Thus, for these particular patterns, a pivot state is reached when the degree of freedom $a_1 = 1$ or 0.

Using the definition of the pivot state, a domain evolution map can be used to show the paths connecting each of the rank-2 laminate domain structures through pivot states, as in figure 5.11. For example, $\{1112\}$ and $\{1221\}$ can evolve into pattern $\{12\}$ or can directly jump to a rank-0 structure $\{1\}$. Domain family $\{1324\}$ has three possible pivot states: they are a single domain state $\{1\}$, domain pattern $\{13\}$ which is a typical 90° domain wall topology, and domain pattern $\{12\}$ with vertical 180° domain wall. Families $\{1213\}$ and $\{1342\}$ both can evolve into a corresponding rank-1 $\{13\}$ pattern or a single domain state $\{1\}$, and so forth.

Next consider the kinetic modelling of these laminate families. The expressions for the rate potential Ψ for the domain topologies considered in the current study are shown in figure 5.12. They are associated with the arrangement of domain walls, but independent of the particular crystal variant present. The single domain state, as shown in figure 5.12(a) representing group $\{1\}$, has no domain walls and thus no evolution is possible. It is also worth noting that the topology shown in figure 5.12(c) has two possible families: $\{12\}$ and $\{13\}$ which have diagonal 180° and 90° domain walls respectively. This implies they have identical forms of rate potential Ψ, as both types of domain interfaces are assumed to have equal domain wall mobility

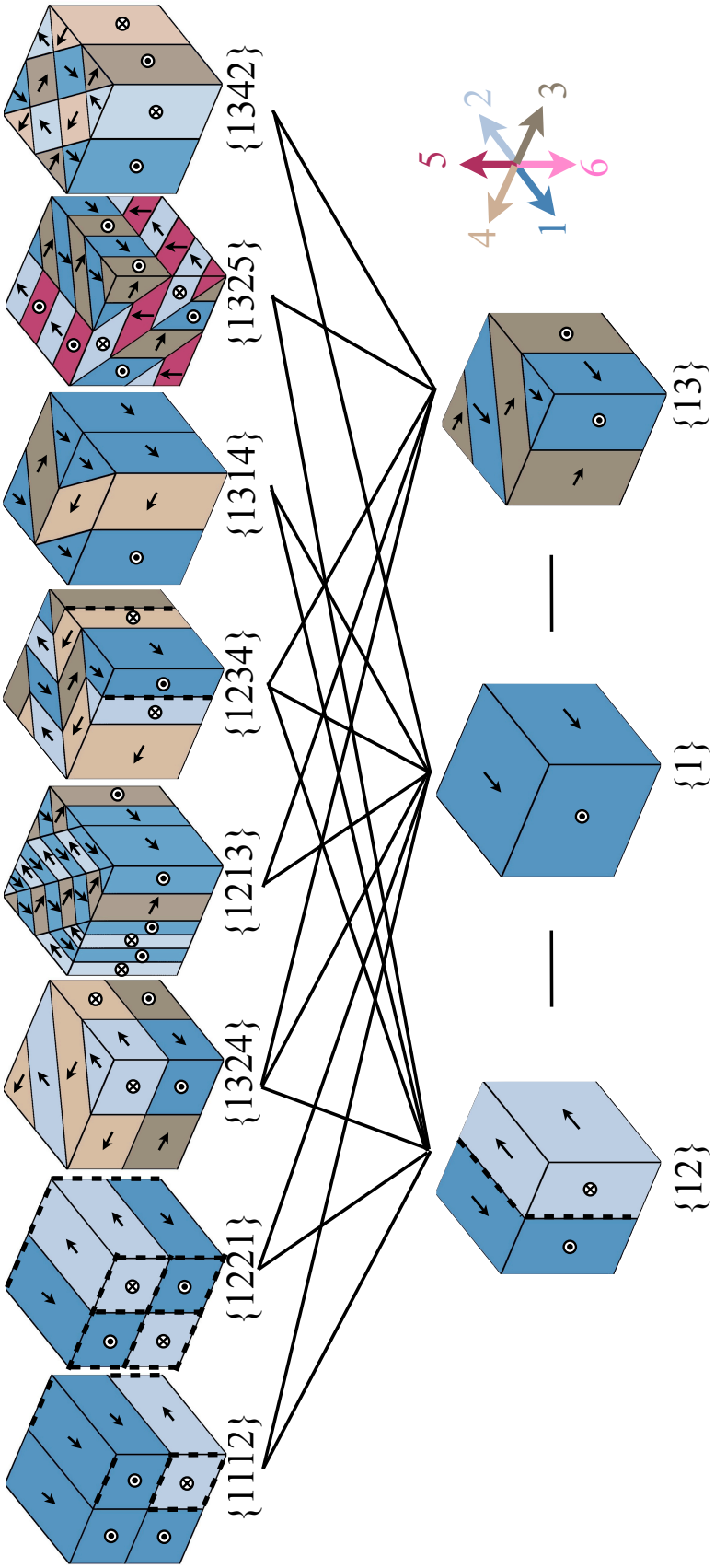

Figure 5.11: The domain evolution map for the switching between patterns which reveals the paths connecting each of the eight families of rank-2 domain pattern through pivot states.

Domain topology	Rate potential Ψ	Possible domain families
(a) 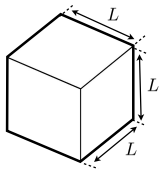	—	{1}
(b) 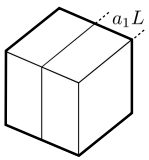	$\frac{L^4}{2m}\dot{a_1}^2$	{12}
(c) 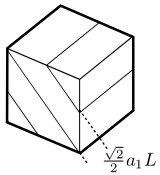	$\frac{\sqrt{2}L^4}{4m}\dot{a_1}^2$	{12}, {13}
(d) 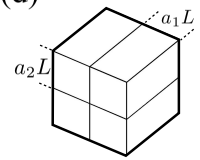	$\frac{L^4}{2m}(\dot{a_1}^2+\dot{a_2}^2)$	{1112}, {1221}
(e) 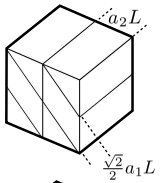	$\frac{L^4}{2m}(\frac{\sqrt{2}}{2}\dot{a_1}^2+\dot{a_2}^2)$	{1112}, {1221}
(f) 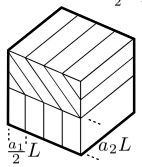	$\frac{L^4}{2m}(\frac{2-2a_2+\sqrt{2}a_2}{4}\dot{a_1}^2+\dot{a_2}^2)$	{1112}, {1221}

Domain topology	Rate potential Ψ	Possible domain families
(g) 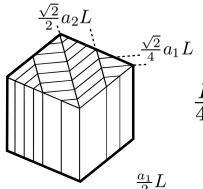	$\frac{L^4}{4m}(\frac{a_2+(1-a_2)\sqrt{2}}{2}\dot{a_1}^2+\sqrt{2}\dot{a_2}^2)$	{1112}, {1221} {1213}
(h) 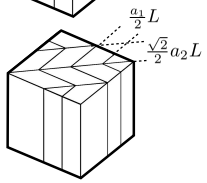	$\frac{L^4}{4m}(\dot{a_1}^2+\sqrt{2}\dot{a_2}^2)$	{1112}, {1221} {1234}
(i) 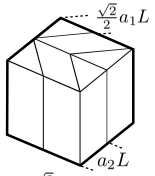	$\frac{L^4}{2m}(\frac{\sqrt{2}}{2}\dot{a_1}^2+\dot{a_2}^2)$	{1112}, {1221} {1314}
(j) 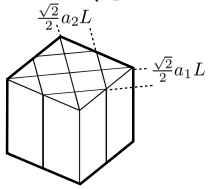	$\frac{\sqrt{2}L^4}{4m}(\dot{a_1}^2+\dot{a_2}^2)$	{1112}, {1221} {1342}
(k) 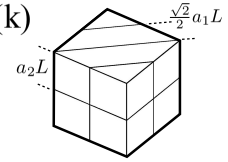	$\frac{L^4}{2m}(\frac{\sqrt{2}}{2}\dot{a_1}^2+\dot{a_2}^2)$	{1234},{1324}
(l) 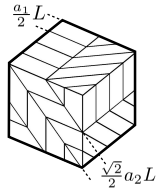	$\frac{\sqrt{2}L^4}{4m}(\frac{1}{2}\dot{a_1}^2+\dot{a_2}^2)$	{1234}, {1325}

Figure 5.12: The expressions of the rate potential Ψ for the 12 domain topologies considered in the current study.

m in the current study. Their rate potential can also be found by setting $\dot{a_1}$ or $\dot{a_2} = 0$ in the expression of the rate potential of their parent topologies, such as the vortex domain pattern shown in figure 5.12(j). For example, the rate potential $\Psi_{\{13\}}$ is equivalent to the rate potential of the vortex structure with Ψ_{5346} in equation (5.21) without the $\dot{a_1}$ terms. It is also interesting to note that the domain topologies shown in figure 5.12(f) and (g) have their rate potentials dependent on the value of degree of freedom a_2, i.e. $\Psi = \Psi(a_2, \dot{a_1}, \dot{a_2})$. This is because the total area of the a_1 domain walls changes with the movement of the a_2 domain wall.

Consider applying the concept of pivot states to the variational model of a $BaTiO_3$ single crystal with a rank-γ ($\gamma = 0...2$) domain pattern subjected to electromechanical loads. At each time step, calculate the rates of the degrees of freedom $\dot{a_r}$ for the current domain pattern, and also for all the domain patterns in connected families on the pivot state map, with rank-$R > \gamma$. For example, at time t, suppose the current domain pattern is rank-1 "13" (containing crystal variants 1 and 3) belonging to family $\{13\}$. There are 10 domain patterns with higher rank to consider in this time step: "1324" in family $\{1324\}$; "1232", "1434" in family $\{1213\}$; three possible "1234" patterns in family $\{1234\}$; "1536" and "1635" in family $\{1325\}$, and finally, "1342", "1432" in family $\{1342\}$. All of these are rank-2 domain structures, which in limiting cases have zero volume fraction of all variants other than 1 and 3. During the current time step, if any one of these structures has a non-zero $\dot{a_r}$ which alters the volume fraction of those variants other than 1 and 3, the nucleation of this domain pattern is assumed to occur. Here, no energetic barrier to the nucleation of new domain patterns has been introduced. Effectively, this is the same as assuming zero surface energy (domain wall energy) associated with nucleation, provided the new pattern is a continuous variation of the previous pattern. The assumption that nucleation presents no energetic barrier is reasonable in the context of experimental observations that fine needle-like or plate-like domains which are precursors for laminate structure can penetrate through ferroelectric crystals at field levels well below the coercive field [112, 113].

If a new pattern forms, this domain pattern then replaces $\{13\}$ and becomes the main state for the next time step. The process of switching between distinct domain patterns is then complete. When the nucleation of a new pattern of domains occurs in the model, one problem is that several patterns may simultaneously become energetically favourable. Which pattern should then be chosen? Observations show that a ferroelectric single crystal usually contains several regions with different laminate domain patterns [114]. Thus, it is reasonable to consider that all the domain patterns which are equally favoured by the applied loads may nucleate in different regions of the crystal. For example, if the applied loads make five domain patterns, say "1324", "1232", "1234", "1342" and "1432" have equal non zero domain velocities for the next time step, we then model the crystal as divided into five equal volume regions containing the five domain patterns. At the next time step, calculation is continued for each of these five regions separately and the overall response of the crystal is found by volume averaging of the response of each individual region. For simplicity, the interaction and compatibility between regions are not considered in the current study, but whenever regions contain identical domain patterns, these regions are assumed to merge by combining their volumes.

Using this model, the hysteresis response of $BaTiO_3$ single crystal under three loading cases can be predicted as shown in figure 5.13. Figure 5.13 shows symmetric dielectric and strain hysteresis loops for all three loading cases. Many features show good agreement with the observations by Burcsu *et al.* [28]. These include the development of kinks (marked K in figure 5.13(c)) and the increasing strain hysteresis with compressive stress. In addition, it is significant that the butterfly loop for the loading case of $\sigma_3 = -1.78\ \mathrm{MPa}$ in figure 5.13(c) suggests an actuation strain of 0.95% which is lower than the theoretical value 1.09% and close to the experimental value reported by Burcsu *et al.* [28] as shown in figure 5.10(c). This decrease of strain output in the model is because some domain patterns nucleate that cannot undergo the complete 90° domain switching. To see this, a schematic domain evolution for the case of $\sigma_3 = -1.78\ \mathrm{MPa}$ generated by the model is shown in figure 5.14.

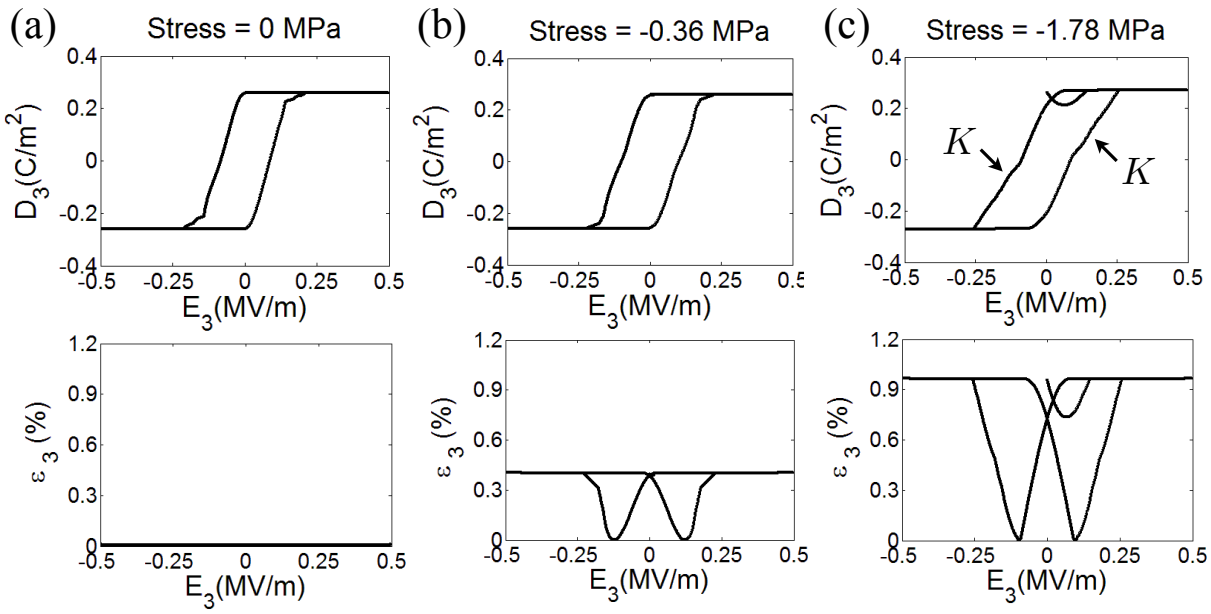

Figure 5.13: Hysteresis responses of the crystal where multiple domain patterns coexist, for all three cases that the crystal is subjected to a compressive stress $\sigma_3 = 0,\ -0.36$, and -1.78 MPa and a cyclic electric field $E_3 = E_0 \sin(2\pi t) \mathrm{MVm}^{-1}$.

It starts from the pattern "5" (figure 5.14(a)). The compressive stress favours many domain patterns with identical domain wall velocities, such as "5126", "5346", "51"...etc. Thus, the material cube is divided into many regions as shown in figure 5.14(b); each thin slice represents one particular domain pattern. As the electric field increases, it drives these patterns back to a single domain state (figure 5.14(c)). When E_3 drops down to around $0.1\mathrm{MVm}^{-1}$, the same structure occurs as it shown in figure 5.14(b) because of similar load conditions at these two time steps. In figure 5.14(e), the volume fraction of crystal variant 5 has decreased significantly. By this stage, some slices of the material cube have reached a pure variant state, such as "1", "2", "3" and "4"; some regions, however, remain rank-2 laminate patterns. This implies that some parts of the crystal have completed 90° switching processes while the domain evolution in other regions was slowed by the particular domain arrangements. For example, the vortex pattern "5126" is visible in figure 5.14(e); this gives a strain output of at most 0.545%, as we discussed previously. Domain patterns of this type reduce the average strain. This result may explain the question of why the reported actuation strains of $BaTiO_3$ are typically smaller than

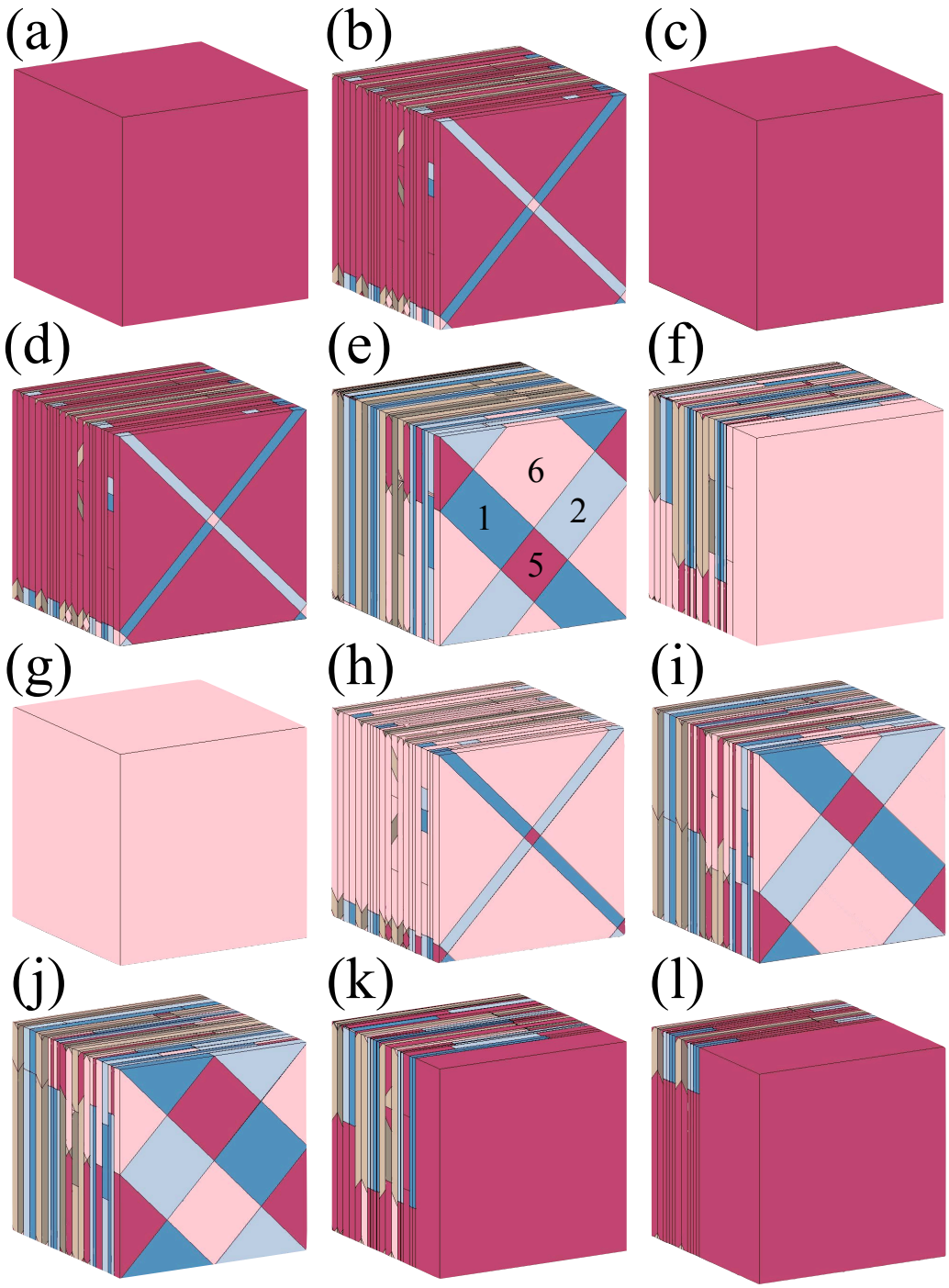

Figure 5.14: The schematic domain evolution in the electric loading cycle under stress $\sigma_3 = -1.78\text{MPa}$. (a) The initial state, single domain state "5". (b) E_3 is around 0.1MVm^{-1}; the material cube is divided into many regions. (c) Electric load overcomes the compressive loads, and domains switch back to single domain state "5". (d) When E_3 drops to around 0.1MVm^{-1}, the same structure occurs as (b) because of similar load conditions. (e) Some regions have complete 90° switching while some parts cannot. (f) When E_3 becomes more negative. (g) Single domain state "6". (h)→(l) The crystal switches back to "5" following a symmetric path of domain pattern evolution to it shown in (c)→(g).

the theoretically predicted value. Next, negative electric field grows or nucleates crystal variant 6 in all regions (figure 5.14(f)) and about $\frac{1}{4}$ of the volume is occupied by a large single domain at this stage. Finally all regions reach single domain state "6" as shown in figure 5.14(g). In figure 5.14(g)→(l), the crystal switches back to single domain state "5" following a symmetric path of domain pattern evolution to that shown in figure 5.14(c)→(g).

A variational model with the concept of pivot states is used to simulate the hysteresis response of a $BaTiO_3$ single crystal, showing good agreement with experimental observations. However, it can be seen in the strain hysteresis loops of figure 5.10 and figure 5.13 that the onset of switching is not well captured by the current model. According to the work done by Shieh *et al.* [109], this feature may be controlled by the "incomplete switching" of the crystal at the saturation state, which is not considered in the present study. Taking this into account could solve the problem of onset of switching, and may reduce the predicted average strain to be closer to the experimental value [28]. In addition, several issues which are ignored in the present work, such as domain wall energy and depolarization energy, may need to be taken into account for more accurate predictions.

6

Conclusions and future work

6.1 Conclusions and discussions

In this thesis, 3-dimensional compatibility conditions were developed for periodic, multi-rank laminate domain configurations of ferroelectric single crystals. Three types of compatibility were identified: average, exact, and disclination-free. Methods have been given for applying the compatibility conditions to the full set of domain walls that exist in a multi-rank laminate. A hierarchical tree diagram was used to represent the laminates, and to define the relations between domains.

Then, an algorithm for finding minimum rank compatible laminate structures was used to study the tetragonal and rhombohedral crystal systems. While many exactly compatible structures were found, the conditions of disclination-free structure proved highly restrictive and few such structures were found. A key result is that domain laminates in both the tetragonal and rhombohedral crystal systems can be designed, which allow the crystal to be poled continuously from a state of zero strain and polarization to a single domain state, while the rank of the laminate never exceeds three. This is significant because it indicates the possibility of poling crystals with very low internal stress induced. At present, crystals commonly crack during poling, or may not reach a fully polarized state. The results from this study suggest some

approaches for solving this problem. Several poling paths are suggested and details of the domain topology along these paths have been found.

Compatibility conditions were also used to classify compatible domain patterns in ferroelectric single crystals. It was found that there are remarkably few distinct domain arrangements that can form as compatible laminates. The eight types of periodic exactly compatible rank-2 laminate in tetragonal crystals are defined and examples from simulation studies and experimental observations confirm their existence. The resulting classification is of direct use in identifying observed domain patterns and provides a basis to search for engineered domain configurations with optimised properties. The procedure can also be applied to other ferroelectric crystal systems. This applicability has been illustrated by classifying the laminate structures in the rhombohedral crystal system.

Next, the exact compatibility conditions were modified for applying to oriented single crystal, ferroelectric films to study the poling ability of the films and the influence of substrate strain. Relatively thick films were studied, with 3-dimensional compatibility constraints. Careful searches for minimum rank exactly compatible laminate domain structures in tetragonal and rhombohedral films of various epitaxial orientations were carried out. Poling paths that could maintain a compatible domain structure while reaching high values of through-thickness polarization were revealed. The utility of such poling routes, if they can be achieved in practice, is that the film maintains a low energy state throughout the process, so that the applied fields should be low and no stresses are induced. However, in some cases the suggested poling routes require unconventional loading such as mechanical shearing or substrate bending. They also need specific initial microstructures, and at present there are no available methods to produce such microstructures reliably. The evolution of domain topology along the suggested poling paths was shown and the greatest value of through-thickness polarization determined for each case. Of interest is the result that optimal poling of the $[011]$ tetragonal film requires a prior shear deformation, but if this can be achieved, a compatible domain structure with polarization

about 42% greater than that of the $[001]$ tetragonal film could be reached. As for rhombohedral films, films with orientation $[001]$ have the maximum through-thickness polarization P_3 compared to those with $[011]$ and $[111]$ orientations. The methodology provides a rapid search for low energy domain arrangements that could be engineered in constrained films. This method could be used to optimise films for memory applications, where easy switching and high polarization are required. Alternatively, it could be used to find microstructures with high stability (low switching ability) but strong, electromechanical coupling, for applications such as sensing or energy harvesting.

In chapters 2-4, the study was purely kinematic in nature. In order to understand the dynamic behaviour of domain wall movement under the given boundary conditions, a kinetic model of microstructure evolution in ferroelectric single crystals was developed. By using the material parameters of barium titanate single crystals, the model has been applied to study the hysteresis response of periodic rank-2 laminate patterns. Microstructural evolution paths along which the domain arrangement maintains compatibility are discussed. Furthermore, a domain evolution map revealing compatible paths between the eight types of rank-2 tetragonal laminate pattern was developed. The domain evolution map was used to capture domain pattern switching through lower rank "pivot states". The hysteresis responses and domain evolution of a barium titanate single crystal under loading similar to that used by Burcsu *et al.* [28] have been simulated. The results have many features in common with the experiment, including some subtle features such as the development of kinks in the dielectric hysteresis, and instability to reach the theoretical maximum strain values during switching. The model can rapidly predict the microstructural evolution in ferroelectrics. However, several simplifications were made: linear kinetics were used; domain wall energy and depolarization energy were also neglected. These features could be modified or incorporated into the given framework of domain evolution.

6.2 Future work

6.2.1 Sharp interface model for multiphase materials and related non-ferroelectrics

In the current kinematic model, the assumption was made that only one type of crystal system is present in the ferroelectric crystal. However, it is possible to form a multiphase domain structure in ferroelectrics. For example, several cases of rhombohedral-tetragonal phase transformation in $BaTiO_3$ and relaxor based materials, such as PMN-PT, are observed [4, 45]. It would be of interest to extend the current model for designing compatible structures where these two crystal phases coexist; however, some complexities would arise. Consider a microstructure with 14 possible crystal variants (6 for tetragonal phase and 8 for rhombohedral phase). The equations provided by equations (2.12)–(2.14) then have several degrees of freedom. This gives multiple solutions for the total volume fraction of each crystal variant under specified average strain and polarization states. Thus, the variant arrangements which allow forming a minimum rank compatible structure need to be identified from all the possible solutions.

Based on the theory provided by Shu and Bhattacharya [24], any pair of domains in tetragonal crystal systems can form a compatible domain wall; the same conclusion can be made in rhombohedral crystal systems. However, a severe restriction is raised if they are in a mixed rhombohedral-tetragonal crystal system. Shu and Bhattacharya assert that a low energy rhombohedral-tetragonal domain wall can only be formed in certain materials with special relations between the crystal parameters: α^t, β^t, p^t, α^{rh}, β^{rh}, p^{rh}. Thus, crystal parameters need to be taken into account. The previous assumption, $\text{tr}(\boldsymbol{\epsilon}) = 0$, in the current model is also not valid for all 14 variants, as there is a volume difference between the phases. However, these restricted conditions may help us to narrow down the uncertainty of multiple solutions from the highly overdetermined system. This task would extend our understanding of the domain structures in some relaxor based materials with ultrahigh strain behaviour [4]. It could also be

of value in understanding the morphotropic phase boundary in polycrystalline materials such as PZT, where coexistence of rhombohedral and tetragonal phases appears to give enhanced electromechanical coupling.

It is also of interest to apply the current sharp interface model to materials which form martensitic microstructures similar to those in ferroelectrics, such as shape memory alloys. Shape memory alloys have the ability to remember and return to their original shape from an arbitrarily deformed state when heat is applied. Such shape-memory effect is widely used in actuators and thin film devices. This effect is caused by a martensitic phase transformation, in which the crystal lattice transforms from the austenite phase (with cubic material unit cells) to the martensite phase (with distorted unit cells). This results in different martensite variants present in the crystal. It appears really similar to the ferroelectric phase transformation. However, there is no polarization induced in this type of material, and only transformation strain states are induced corresponding to each of the variants. This presents an interesting challenge, because the absence of polarization reduces compatibility constraints, so that typically there are two compatible interface orientations for a given pair of symmetry related crystal variants. So methods are needed for dealing with the additional permutations of microstructure.

In recent years, many phase field models have been developed to predict microstructures in shape memory materials [84, 115–118]. However, 2-dimensional problems or small regions of interest are typically considered. Shape memory alloys commonly adopt monoclinic or orthorhombic-monoclinic crystal systems which have 12 and 18 crystal variants, respectively. Such a great number of variants typically makes phase field approaches for martensitic materials even more computationally intensive. Sharp interface approaches which can significantly reduce the computational requirements then become more important for modelling 3-dimensional microstructures in shape memory materials. However, typical sharp interface approaches in the literature [86, 91] assume particular twin arrangements. Therefore, it is worth studying low-energy microstructures which can form in shape memory alloys for given boundary conditions

based on the compatibility conditions and methodologies provided in chapters 2 and 3. The results could provide a valuable overview picture of microstructures in shape memory alloys and guidelines for the design of shape memory alloys.

6.2.2 Sharp interface model for true thin film applications

In chapter 4, we considered relatively thick films with low energy microstructures which satisfy compatibility conditions in a 3-dimensional sense. However, in a true thin film, the strain compatibility constraints, equation (2.6), can be relaxed in the out-of-plane direction as the deformation energy becomes much smaller than the interfacial and membrane energies [75]. As a consequence, thin films can allow a greater range of low energy domain structures than bulk crystals. This is particularly beneficial to domain engineering which rearranges the structures for optimised properties. Thus, it is of interest to modify the current model to explore the low energy domain structures in thin films and compare them with the findings in chapter 4. The results should provide a better understanding of the relationship between film thickness and the formation of possible microstructures.

Moreover, all the models developed so far focus on the case that the materials are at an isothermal condition. Thus, the temperature dependence of microstructures are not considered in this thesis. However, this is in fact an important issue when considering the performance and the operating temperature range of ferroelectric film devices. The observation done by Surowiak *et al.* [119] shows that the domain pattern and the mean domain width in a $(Ba_{0.7}Sr_{0.3})TiO_3$ film have significant changes as the temperature rises from $293\ \mathrm{K}$ to $403\ \mathrm{K}$. The film was also found to be under a strong in-plane compression during this process. Pertsev *et al.* [80, 120] develop a thermodynamic framework to generate domain stability maps and phase diagrams revealing the correlation between temperature and the lattice misfit strain for $BaTiO_3$ and $PbTiO_3$. Thus, it is of interest to take the temperature dependence of crystal parameters into account in the current sharp interface model, and search low energy domain structures in thin films subjected to

different temperatures. This could produce microstructure maps which can provide a guideline for designing thin film devices with a wider operating temperature range.

6.2.3 Kinetic modelling of laminates

The kinetic model proposed in chapter 5 can rapidly predict the electromechanical behaviour of a ferroelectric single crystal, and reproduce many features observed in experimental works. However, it limits the consideration to domain structures with rank lower than 3. In some cases, the limitation to rank-2 structure produces "clamping" effects. For example, if a tetragonal single crystal with an initial domain pattern "1234", containing crystal variants with only x–y polarization directions, is subjected to an electric field along the z-direction and no stress is applied, then the model suggests that there is no hysteresis response. This is because a rank-3 laminate would be needed in order to introduce the additional domain wall for switching into the z-direction. To achieve this, we could apply the method introduced in section 3.5 to classify all possible rank-3 laminate patterns. But for ferroelectrics in the tetragonal crystal system, there are in total $6^8 = 1679616$ possible arrangements of crystal variant in the lowest level of a rank-3 tree diagram. Thus some new thinking is needed to simplify the problem. Although some complexities may arise when including rank-3 laminates into the existing kinetic framework, the resulting model could be better able to predict the hysteresis response of ferroelectrics in multiaxial loading conditions.

Another interesting task for further work is to improve the method used in section 5.3, where the overall hysteresis responses are obtained by volume averaging the responses of a set of patterns that are energetically favourable under the applied loads. The interaction and compatibility between these domain patterns were not considered in the current study. In order to take these effects into account, a model which combines the present sharp interface method and a 3-dimensional phase field approach could be developed. Phase field approaches can predict the evolution of domain structure from a non-equilibrium state towards an equilibrium

state without prior assumptions of domain pattern. However, this is typically a computationally intensive approach. Thus, a possible strategy is to convert the domain patterns generated by the sharp interface method into an input for the phase field model as an initial state. This initial state could have several regions containing exactly compatible domain patterns, meeting at incompatible (arbitrary) interfaces. As the compatibility across the boundaries where these patterns meet is not guaranteed, the crystal would start at a non-equilibrium state. However, the phase field approach could then model the evolution of microstructure by minimising the total energy. If the structure evolves into a periodic multi-rank laminate structure, the current domain pattern could be converted back to an input for a sharp interface model for efficiency. The proposed "integrated model" could be more accurate and reliable than the current sharp interface model but potentially also more efficient than conventional phase field models.

A

Appendix

A.1 The effective material properties of ferroelectric crystals

In this section, we describe the method proposed by Li and Liu [26] to calculate the effective material properties. In chapter 1, the tensor form of constitutive equations for piezoelectrics are shown in equations (1.1) and (1.2). They can be shown in matrix form:

$$\begin{bmatrix} \epsilon_1 \\ \epsilon_2 \\ \epsilon_3 \\ \epsilon_4 \\ \epsilon_5 \\ \epsilon_6 \\ D_1 \\ D_2 \\ D_3 \end{bmatrix} = \begin{bmatrix} S_{11} & S_{12} & S_{13} & S_{14} & S_{15} & S_{16} & d_{11} & d_{21} & d_{31} \\ S_{12} & S_{22} & S_{23} & S_{24} & S_{25} & S_{26} & d_{12} & d_{22} & d_{32} \\ S_{13} & S_{23} & S_{33} & S_{34} & S_{35} & S_{36} & d_{13} & d_{23} & d_{33} \\ S_{14} & S_{24} & S_{34} & S_{44} & S_{45} & S_{46} & d_{14} & d_{24} & d_{34} \\ S_{15} & S_{25} & S_{35} & S_{45} & S_{55} & S_{56} & d_{15} & d_{25} & d_{35} \\ S_{16} & S_{26} & S_{36} & S_{46} & S_{56} & S_{66} & d_{16} & d_{26} & d_{36} \\ d_{11} & d_{12} & d_{13} & d_{14} & d_{15} & d_{16} & \kappa_{11} & \kappa_{12} & \kappa_{13} \\ d_{21} & d_{22} & d_{23} & d_{24} & d_{25} & d_{26} & \kappa_{12} & \kappa_{22} & \kappa_{23} \\ d_{31} & d_{32} & d_{33} & d_{34} & d_{35} & d_{36} & \kappa_{13} & \kappa_{23} & \kappa_{33} \end{bmatrix} \begin{bmatrix} \sigma_1 \\ \sigma_2 \\ \sigma_3 \\ \sigma_4 \\ \sigma_5 \\ \sigma_6 \\ E_1 \\ E_2 \\ E_3 \end{bmatrix} \tag{A.1}$$

Then, Li and Liu rearrange and simplise equation (A.1) as

$$\begin{bmatrix} \mathbf{Y} \\ \mathbf{Z} \end{bmatrix} = \begin{bmatrix} \mathbf{A} & \mathbf{B} \\ \mathbf{B}^T & \mathbf{N} \end{bmatrix} \begin{bmatrix} \mathbf{F} \\ \mathbf{G} \end{bmatrix} \tag{A.2}$$

where superscript T indicates the operation of matrix transpose and

$$\mathbf{Y} = \begin{bmatrix} \epsilon_1 \\ \epsilon_2 \\ \epsilon_6 \\ D_3 \end{bmatrix}, \quad \mathbf{Z} = \begin{bmatrix} \epsilon_3 \\ \epsilon_4 \\ \epsilon_5 \\ D_1 \\ D_2 \end{bmatrix}, \quad \mathbf{F} = \begin{bmatrix} \sigma_1 \\ \sigma_2 \\ \sigma_6 \\ E_3 \end{bmatrix}, \quad \mathbf{G} = \begin{bmatrix} \sigma_3 \\ \sigma_4 \\ \sigma_5 \\ E_1 \\ E_2 \end{bmatrix},$$

$$\mathbf{A} = \begin{bmatrix} S_{11} & S_{12} & S_{16} & d_{31} \\ S_{12} & S_{22} & S_{26} & d_{32} \\ S_{16} & S_{26} & S_{66} & d_{36} \\ d_{31} & d_{32} & d_{36} & \kappa_{33} \end{bmatrix}, \quad \mathbf{B} = \begin{bmatrix} S_{13} & S_{14} & S_{15} & d_{11} & d_{21} \\ S_{23} & S_{24} & S_{25} & d_{12} & d_{22} \\ S_{36} & S_{46} & S_{56} & d_{16} & d_{26} \\ d_{33} & d_{34} & d_{35} & \kappa_{13} & \kappa_{23} \end{bmatrix},$$

$$\mathbf{N} = \begin{bmatrix} S_{33} & S_{34} & S_{35} & d_{13} & d_{23} \\ S_{34} & S_{44} & S_{45} & d_{14} & d_{24} \\ S_{35} & S_{45} & S_{55} & d_{15} & d_{25} \\ d_{13} & d_{14} & d_{15} & \kappa_{11} & \kappa_{12} \\ d_{23} & d_{24} & d_{25} & \kappa_{12} & \kappa_{22} \end{bmatrix}.$$

Now consider a laminate structure with two crystal variants present in the ferroelectric crystal. In order to simplify the calculation, the direction of the interface normal is chosen as the z-axis in local coordinate system. Therefore, proper rotating operations need to be undergone for the global material properties of each crystal variant. For the variant k, the constitutive

equation, equation (A.2), is written as:

$$\begin{bmatrix} \mathbf{Y}_k \\ \mathbf{Z}_k \end{bmatrix} = \begin{bmatrix} \mathbf{A}_k & \mathbf{B}_k \\ \mathbf{B}_k^T & \mathbf{N}_k \end{bmatrix} \begin{bmatrix} \mathbf{F}_k \\ \mathbf{G}_k \end{bmatrix} \tag{A.3}$$

The combination of two crystal variants results in a heterogeneous electromechanical field distribution in the crystal. However, the field is required to be continuous across the interface that

$$\mathbf{Y}_1 = \mathbf{Y}_2 = \overline{\mathbf{Y}}, \quad \mathbf{G}_1 = \mathbf{G}_2 = \overline{\mathbf{G}} \tag{A.4}$$

where the overhead bar indicates the volume averaged field variables in the laminate. By using equations (A.3) and (A.4), we can obtain $\mathbf{F}_k$ and $\mathbf{Z}_k$ for crystal variant k

$$\begin{aligned} \mathbf{F}_k &= \mathbf{A}_k^{-1}\overline{\mathbf{Y}} - \mathbf{A}_k^{-1}\mathbf{B}_k\overline{\mathbf{G}} \\ \mathbf{Z}_k &= \mathbf{B}_k^T\mathbf{F}_k + \mathbf{N}_k\overline{\mathbf{G}} = \mathbf{B}_k^T\mathbf{A}_k^{-1}\overline{\mathbf{Y}} + (\mathbf{N}_k - \mathbf{B}_k^T\mathbf{A}_k^{-1}\mathbf{B}_k)\overline{\mathbf{G}} \end{aligned} \tag{A.5}$$

This results in

$$\begin{aligned} \overline{\mathbf{F}} &= \langle \mathbf{A}^{-1} \rangle \overline{\mathbf{Y}} - \langle \mathbf{A}^{-1}\mathbf{B} \rangle \overline{\mathbf{G}} \\ \overline{\mathbf{Z}} &= \langle \mathbf{B}^T\mathbf{A}^{-1} \rangle \overline{\mathbf{Y}} + (\langle \mathbf{N} \rangle - \langle \mathbf{B}^T\mathbf{A}^{-1}\mathbf{B} \rangle)\overline{\mathbf{G}} \end{aligned} \tag{A.6}$$

where $\langle\ \rangle$ indicates the volume averaged physical properties. It is possible to rearrange further

$$\begin{aligned} \overline{\mathbf{Y}} &= \langle \mathbf{A}^{-1} \rangle^{-1}\overline{\mathbf{F}} + \langle \mathbf{A}^{-1} \rangle^{-1}\langle \mathbf{A}^{-1}\mathbf{B} \rangle \overline{\mathbf{G}} \\ \overline{\mathbf{Z}} &= \langle \mathbf{B}^T\mathbf{A}^{-1} \rangle \langle \mathbf{A}^{-1} \rangle^{-1}\overline{\mathbf{F}} + (\langle \mathbf{B}^T\mathbf{A}^{-1} \rangle \langle \mathbf{A}^{-1} \rangle^{-1}\langle \mathbf{A}^{-1}\mathbf{B} \rangle + \langle \mathbf{N} \rangle - \langle \mathbf{B}^T\mathbf{A}^{-1}\mathbf{B} \rangle)\overline{\mathbf{G}} \end{aligned} \tag{A.7}$$

Now the overall effective properties for this rank-1 laminate are obtained

$$\begin{aligned} \mathbf{A}^* &= \langle \mathbf{A}^{-1} \rangle^{-1} \\ \mathbf{B}^* &= \langle \mathbf{A}^{-1} \rangle^{-1}\langle \mathbf{A}^{-1}\mathbf{B} \rangle \\ \mathbf{B}^{T*} &= \langle \mathbf{B}^T\mathbf{A}^{-1} \rangle \langle \mathbf{A}^{-1} \rangle^{-1} \\ \mathbf{N}^* &= \langle \mathbf{B}^T\mathbf{A}^{-1} \rangle \langle \mathbf{A}^{-1} \rangle^{-1}\langle \mathbf{A}^{-1}\mathbf{B} \rangle + \langle \mathbf{N} \rangle - \langle \mathbf{B}^T\mathbf{A}^{-1}\mathbf{B} \rangle \end{aligned} \tag{A.8}$$

The same calculation procedure can be applied recursively to multi-rank laminate structures provided the separation of length scales between different levels. This condition makes a lower level laminate can be treated as a homogeneous medium with the calculated effective properties when considering the effective behaviour of the higher level laminate.

References

[1] G. Arlt and P. Sasko. Domain configuration and equilibrium size of domains in $BaTiO_3$ ceramics. *Journal of Applied Physics*, 51(9):4956, 1980.

[2] G. Arlt. Twinning in ferroelectric and ferroelastic ceramics: stress relief. *Journal of Materials Science*, 25(6):2655–2666, 1990.

[3] N. A. Pertsev and G. Arlt. Internal stresses and elastic energy in ferroelectric and ferroelastic ceramics: Calculations by the dislocation method. *Ferroelectrics*, 123(1):27–44, 1991.

[4] S. E. Park and T. R. Shrout. Ultrahigh strain and piezoelectric behavior in relaxor based ferroelectric single crystals. *Journal of Applied Physics*, 82(4):1804, 1997.

[5] T. Liu and C. S. Lynch. Domain engineered relaxor ferroelectric single crystals. *Continuum Mechanics and Thermodynamics*, 18(1-2):119–135, 2006.

[6] L. Q. Chen. Phase-field models for microstructure evolution. *Annual Review of Materials Research*, 32(1):113–140, 2002.

[7] Y. Su and C. M. Landis. Continuum thermodynamics of ferroelectric domain evolution: Theory, finite element implementation, and application to domain wall pinning. *Journal of the Mechanics and Physics of Solids*, 55(2):280–305, 2007.

[8] S. Choudhury, L. Q. Chen, and Y. L. Li. Correlation between number of ferroelectric variants and coercive field of lead zirconate titanate single crystals. *Applied Physics Letters*, 91(3):032902, 2007.

[9] J. Slutsker, A. Artemev, and A. Roytburd. Phase-field modeling of domain structure of confined nanoferroelectrics. *Physical Review Letters*, 100(8):087602, 2008.

[10] J. X. Zhang, R. Wu, S. Choudhury, Y. L. Li, S. Y. Hu, and L. Q. Chen. Three-dimensional phase-field simulation of domain structures in ferroelectric islands. *Applied Physics Letters*, 92(12):122906, 2008.

[11] H. L. Hu and L. Q. Chen. Three-dimensional computer simulation of ferroelectric domain formation. *Journal of the American Ceramic Society*, 81(3):492–500, 1998.

[12] K. Dayal and K. Bhattacharya. A real-space non-local phase-field model of ferroelectric domain patterns in complex geometries. *Acta Materialia*, 55(6):1907–1917, 2007.

[13] Y. C. Shu, J. H. Yen, H. Z. Chen, J. Y. Li, and L. J. Li. Constrained modeling of domain patterns in rhombohedral ferroelectrics. *Applied Physics Letters*, 92(5):052909, 2008.

[14] D. Schrade, R. Mueller, B. Xu, and D. Gross. Domain evolution in ferroelectric materials: A continuum phase field model and finite element implementation. *Computer Methods in Applied Mechanics and Engineering*, 196(41-44):4365–4374, 2007.

[15] S. Choudhury, Y. L. Li, C. E. Krill III, and L. Q. Chen. Phase-field simulation of polarization switching and domain evolution in ferroelectric polycrystals. *Acta Materialia*, 53(20):5313–5321, 2005.

[16] W. Cao and L. E. Cross. Theory of tetragonal twin structures in ferroelectric perovskites with a first-order phase transition. *Physical Review B*, 44(1):5, 1991.

[17] J. Wang, S. Q. Shi, L. Q. Chen, Y. Li, and T. Y. Zhang. Phase-field simulations of ferroelectric/ferroelastic polarization switching. *Acta Materialia*, 52(3):749–764, 2004.

[18] W. Zhang and K. Bhattacharya. A computational model of ferroelectric domains. part I: model formulation and domain switching. *Acta Materialia*, 53(1):185–198, 2005.

[19] W. Zhang and K. Bhattacharya. A computational model of ferroelectric domains. part II: grain boundaries and defect pinning. *Acta Materialia*, 53(1):199–209, 2005.

[20] A. Kontsos and C. M. Landis. Computational modeling of domain wall interactions with dislocations in ferroelectric crystals. *International journal of solids and structures*, 46(6):1491, 2009.

[21] A. Kontsos and C. M. Landis. Phase-Field modeling of domain structure energetics and evolution in ferroelectric thin films. *Journal of applied mechanics*, 77:041014, 2010.

[22] Y. C. Shu. Application of energy-minimizing laminates to the modeling of ferroelectric domain and switching. In *Finite Plasticity and Visco-Plasticity of Conventional and Emerging Materials*, pages 142–144, Jonesboro, AR, USA, 2010.

[23] G. H. Haertling. Ferroelectric ceramics: History and technology. *Journal of the American Ceramic Society*, 82(4):797–818, 2004.

[24] Y. C. Shu and K. Bhattacharya. Domain patterns and macroscopic behaviour of ferroelectric materials. *Philosophical Magazine Part B*, 81(12):2021–2054, 2001.

[25] IEEE. IEEE standard on piezoelectricity. *ANSI/IEEE Std 176-1987*, 1(1):1, 1988.

[26] J. Li and D. Liu. On ferroelectric crystals with engineered domain configurations. *Journal of the Mechanics and Physics of Solids*, 52(8):1719–1742, 2004.

[27] C. S. Lynch, W. Chen, and T. Liu. Multiaxial constitutive behavior of ferroelectric materials. In *Proceedings of SPIE*, pages 245–254, Newport Beach, CA, USA, 2000.

[28] E. Burcsu, G. Ravichandran, and K. Bhattacharya. Large electrostrictive actuation of barium titanate single crystals. *Journal of the Mechanics and Physics of Solids*, 52(4):823–846, 2004.

[29] J. E. Huber. Micromechanical modelling of ferroelectrics. *Current Opinion in Solid State and Materials Science*, 9(3):100–106, 2005.

[30] S. C. Hwang, J. E. Huber, R. M. McMeeking, and N. A. Fleck. The simulation of switching in polycrystalline ferroelectric ceramics. *Journal of Applied Physics*, 84(3):1530, 1998.

[31] W. Lu, D. N. Fang, C. Q. Li, and K. C. Hwang. Nonlinear electric-mechanical behavior and micromechanics modelling of ferroelectric domain evolution. *Acta Materialia*, 47(10):2913–2926, 1999.

[32] T. Michelitsch and W. S. Kreher. A simple model for the nonlinear material behavior of ferroelectrics. *Acta Materialia*, 46(14):5085–5094, 1998.

[33] H. Kessler and H. Balke. On the local and average energy release in polarization switching phenomena. *Journal of the Mechanics and Physics of Solids*, 49(5):953–978, 2001.

[34] J. E. Huber, N. A. Fleck, C. M. Landis, and R. M. McMeeking. A constitutive model for ferroelectric polycrystals. *Journal of the Mechanics and Physics of Solids*, 47(8):1663–1697, 1999.

[35] C. M. Landis and R. M. McMeeking. A self-consistent constitutive model for switching in polycrystalline barium titanate. *Ferroelectrics*, 255(1):13–34, 2001.

[36] J. Rödel and W. S. Kreher. Self-consistent modelling of non-linear effective properties of polycrystalline ferroelectric ceramics. *Computational Materials Science*, 19(1-4):123–132, 2000.

[37] F. Li and D. Fang. Simulations of domain switching in ferroelectrics by a three-dimensional finite element model. *Mechanics of Materials*, 36(10):959–973, 2004.

[38] S. Anteboth, A. Brückner-Foit, M. J. Hoffmann, U. Sutter, Th. Schimmel, and M. Müller. Electromechanical behaviour of PZT with real domain structure. *Computational Materials Science*, 41(3):420–429, 2008.

[39] A. Pathak and R. M. McMeeking. Three-dimensional finite element simulations of ferroelectric polycrystals under electrical and mechanical loading. *Journal of the Mechanics and Physics of Solids*, 56(2):663–683, 2008.

[40] A. Haug, J. E. Huber, P. R. Onck, and E. V. Giessen. Multi-grain analysis versus self-consistent estimates of ferroelectric polycrystals. *Journal of the Mechanics and Physics of Solids*, 55(3):648–665, 2007.

[41] A. Haug, P. R. Onck, and E. V. Giessen. Development of inter- and intragranular stresses during switching of ferroelectric polycrystals. *International Journal of Solids and Structures*, 44(6):2066–2078, 2007.

[42] S. Wada, S. Suzuki, T. Noma, T. Suzuki, M. Osada, M. Kakihana, S. E. Park, L. E. Cross, and T. R. Shrout. Enhanced piezoelectric property of barium titanate single crystals with engineered domain configurations. *Japanese Journal of Applied Physics*, 38(Part 1, No. 9B):5505–5511, 1999.

[43] A. J. Bell. Phenomenologically derived electric field-temperature phase diagrams and piezoelectric coefficients for single crystal barium titanate under fields along different axes. *Journal of Applied Physics*, 89(7):3907, 2001.

[44] J. Yin and W. Cao. Observation and analysis of domain configurations in domain engineered PZN-PT single crystals. *Ferroelectrics*, 251(1):93, 2001.

[45] S. E. Park, S. Wada, L. E. Cross, and T. R. Shrout. Crystallographically engineered $BaTiO_3$ single crystals for high-performance piezoelectrics. *Journal of Applied Physics*, 86(5):2746, 1999.

[46] X. Zeng and R. K. N. D. Rajapakse. Eshelby tensor for piezoelectric inclusion and application to modeling of domain switching and evolution. *Acta Materialia*, 51(14):4121–4134, 2003.

[47] M. Molotskii. Forward motion of ferroelectric domain walls. *Philosophical magazine letters*, 83(12):763, 2003.

[48] N. T. Tsou and J. E. Huber. A variational model of ferroelectric rank-2 laminate domain structures. In *Proceedings of SPIE*, pages 76440B–76440B–8, San Diego, CA, USA, 2010.

[49] N. T. Tsou and J. E. Huber. Domain evolution of herringbone structures in ferroelectric single crystals. *ASME 2010 Conference on Smart Materials, Adaptive Structures and Intelligent Systems.*, 1(SMASIS2010-3819), 2010.

[50] J. M. Ball and R. D. James. Fine phase mixtures as minimizers of energy. *Archive for Rational Mechanics and Analysis*, 100(1):13–52, 1987.

[51] K. Bhattacharya. Comparison of the geometrically nonlinear and linear theories of martensitic transformation. *Continuum Mechanics and Thermodynamics*, 5(3):205–242, 1993.

[52] A. DeSimone and R. D. James. A constrained theory of magnetoelasticity. *Journal of the Mechanics and Physics of Solids*, 50(2):283–320, 2002.

[53] J. Fousek and P. Mokry. Stress-Free domain quadruplets in ferroics. *Ferroelectrics*, 323(1):3–9, 2005.

[54] D. Savytskii and U. Bismayer. Strain at junctions in multidomain configurations. *Phase transitions*, 81(5):431, 2008.

[55] B. Meyer and D. Vanderbilt. Ab initio study of ferroelectric domain walls in $PbTiO_3$. *Physical Review B*, 65(10):104111, 2002.

[56] I. I. Naumov, L. Bellaiche, and H. X. Fu. Unusual phase transitions in ferroelectric nanodisks and nanorods. *Nature*, 432(7018):737–740, 2004.

[57] R. E. Cohen and H. Krakauer. Lattice dynamics and origin of ferroelectricity in $BaTiO_3$: linearized-augmented-plane-wave total-energy calculations. *Physical Review B*, 42(10):6416, 1990.

[58] L. M. Eng, J. Fousek, and P. Gunter. Ferroelectric domains and domain boundaries observed by scanning force microscopy. *Ferroelectrics*, 191(1):211–218, 1997.

[59] E. Fried and M. E. Gurtin. Continuum theory of thermally induced phase transitions based on an order parameter. *Physica D: Nonlinear Phenomena*, 68(3-4):326–343, 1993.

[60] E. Fried and M. E. Gurtin. Dynamic solid-solid transitions with phase characterized by an order parameter. *Physica D: Nonlinear Phenomena*, 72(4):287–308, 1994.

[61] R. E. Loge and Z. Suo. Nonequilibrium thermodynamics of ferroelectric domain evolution. *Acta Materialia*, 44(8):3429–3438, 1996.

[62] G. J. Weng and D. T. Wong. Thermodynamic driving force in ferroelectric crystals with a rank-2 laminated domain pattern, and a study of enhanced electrostriction. *Journal of the Mechanics and Physics of Solids*, 57(3):571–597, 2009.

[63] J. E. Huber and A. C. F. Cocks. A variational model of ferroelectric microstructure. In *Proceedings of ASME 2008 Conference on Smart Materials, Adaptive Structures and Intelligent Systems.*, volume 1, pages SMASIS2008–360, 2008.

[64] J. H. Yen, Y. C. Shu, J. Shieh, and J. H. Yeh. A study of electromechanical switching in ferroelectric single crystals. *Journal of the Mechanics and Physics of Solids*, 56(6):2117–2135, 2008.

[65] J. D. Eshelby. The elastic energy-momentum tensor. *Journal of Elasticity*, 5(3-4):321–335, 1975.

[66] H. Kessler and H. Balke. A continuum analysis of the driving force of ferroelectric/-ferroelastic domain wall motions. *Journal of the Mechanics and Physics of Solids*, 54(1):113–127, 2006.

[67] S. Kim. A rate-dependent thermo-electro-mechanical free energy model for perovskite type single crystals. *International Journal of Engineering Science*, 45(9):770–785, 2007.

[68] S. P. A. Gill, M. G. Cornforth, and A. C. F. Cocks. Modelling microstructure evolution in engineering materials. *International Journal of Plasticity*, 17(4):669–690, 2001.

[69] D. Shilo, E. Burcsu, G. Ravichandran, and K. Bhattacharya. A model for large electrostrictive actuation in ferroelectric single crystals. *International Journal of Solids and Structures*, 44(6):2053–2065, 2007.

[70] N. Setter, D. Damjanovic, L. Eng, G. Fox, S. Gevorgian, S. Hong, A. Kingon, H. Kohlstedt, N. Y. Park, G. B. Stephenson, I. Stolitchnov, A. K. Taganstev, D. V. Taylor, T. Yamada, and S. Streiffer. Ferroelectric thin films: Review of materials, properties, and applications. *Journal of Applied Physics*, 100(5):051606, 2006.

[71] A. L. Roytburd. Thermodynamics of polydomain heterostructures. I. effect of macrostresses. *Journal of Applied Physics*, 83(1):228, 1998.

[72] J. N. Hanson, B. J. Rodriguez, R. J. Nemanich, and A. Gruverman. Fabrication of metallic nanowires on a ferroelectric template via photochemical reaction. *Nanotechnology*, 17(19):4946–4949, 2006.

[73] Y. L. Li, S. Y. Hu, Z. K. Liu, and L. Q. Chen. Effect of substrate constraint on the stability and evolution of ferroelectric domain structures in thin films. *Acta Materialia*, 50(2):395–411, 2002.

[74] K. J. Choi, M. Biegalski, Y. L. Li, A. Sharan, J. Schubert, R. Uecker, P. Reiche, Y. B. Chen, X. Q. Pan, V. Gopalan, L.Q. Chen, D. G. Schlom, and C. B. Eom. Enhancement of ferroelectricity in strained $BaTiO_3$ thin films. *Science*, 306(5698):1005 –1009, 2004.

[75] K. Bhattacharya and R. D. James. A theory of thin films of martensitic materials with applications to microactuators. *Journal of the Mechanics and Physics of Solids*, 47(3):531–576, 1999.

[76] V. G. Koukhar, N. A. Pertsev, and R. Waser. In-plane polarization states and their instabilities in polydomain epitaxial ferroelectric thin films. *Applied Physics Letters*, 78(4):530, 2001.

[77] A. L. Roytburd. Thermodynamics of polydomain heterostructures. II. effect of microstresses. *Journal of Applied Physics*, 83(1):239, 1998.

[78] S. P. Alpay and A. L. Roytburd. Thermodynamics of polydomain heterostructures. III. domain stability map. *Journal of Applied Physics*, 83(9):4714, 1998.

[79] J. S. Speck and W. Pompe. Domain configurations due to multiple misfit relaxation mechanisms in epitaxial ferroelectric thin films. i. theory. *Journal of Applied Physics*, 76(1):466, 1994.

[80] N. A. Pertsev and V. G. Koukhar. Polarization instability in polydomain ferroelectric epitaxial thin films and the formation of heterophase structures. *Physical Review Letters*, 84(16):3722, 2000.

[81] Y. L. Li, S. Y. Hu, Z. K. Liu, and L. Q. Chen. Phase-field model of domain structures in ferroelectric thin films. *Applied Physics Letters*, 78(24):3878, 2001.

[82] J. E. Huber. Micromechanical modeling of ferroelectric films. *Journal of Materials Research*, 21(3):557–562, 2006.

[83] Y. L. Li and L. Q. Chen. Temperature-strain phase diagram for $BaTiO_3$ thin films. *Applied Physics Letters*, 88(7):072905, 2006.

[84] Y. C. Shu and J. H. Yen. Multivariant model of martensitic microstructure in thin films. *Acta Materialia*, 56(15):3969–3981, September 2008.

[85] A. L. Roytburd, S. P. Alpay, L. A. Bendersky, V. Nagarajan, and R. Ramesh. Three-domain architecture of stress-free epitaxial ferroelectric films. *Journal of Applied Physics*, 89(1):553, 2001.

[86] A. L. Roytburd, T. S. Kim, Quanmin Su, J. Slutsker, and M. Wuttig. Martensitic transformation in constrained films. *Acta Materialia*, 46(14):5095–5107, 1998.

[87] I. Pane, N. A. Fleck, J. E. Huber, and D. P. Chu. Effect of geometry upon the performance of a thin film ferroelectric capacitor. *International Journal of Solids and Structures*, 45(7-8):2024–2041, 2008.

[88] I. Pane, N. A. Fleck, D. P. Chu, and J. E. Huber. The influence of mechanical constraint upon the switching of a ferroelectric memory capacitor. *European Journal of Mechanics - A/Solids*, 28(2):195–201, 2009.

[89] K. Bhattacharya. *Microstructure of martensite: why it forms and how it gives rise to the shape-memory effect*. Oxford University Press, 2003.

[90] M. E. Gurtin. *An introduction to continuum mechanics*. Academic Press, 1981.

[91] G. H. Goldsztein. The effective energy and laminated microstructures in martensitic phase transformations. *Journal of the Mechanics and Physics of Solids*, 49(4):899–925, 2001.

[92] M. Stengel, P. Aguado-Puente, N. A. Spaldin, and J. Junquera. Band alignment at metal/ferroelectric interfaces: Insights and artifacts from first principles. *Physical Review B*, 83(23):235112, 2011.

[93] J. Rödel. Effective intrinsic linear properties of laminar piezoelectric composites and simple ferroelectric domain structures. *Mechanics of Materials*, 39(4):302–325, 2007.

[94] A. Schilling, T. B. Adams, M. M. Saad, P. Baxter, F. D. Morrison, G. Catalan, J. F. Scott, R. M. Bowman, and J. M. Gregg. Nanoscale ferroelectrics machined from single crystals. *Integrated Ferroelectrics*, 92(1):53–64, 2007.

[95] T. Granzow, A. B. Kounga, E. Aulbach, and J. Rödel. Electromechanical poling of piezoelectrics. *Applied Physics Letters*, 88(25):252907, 2006.

[96] S. Y. Cheng, N. J. Ho, and H. Y. Lu. Transformation-Induced twinning: The 90° and 180° ferroelectric domains in tetragonal barium titanate. *Journal of the American Ceramic Society*, 89(7):2177, 2006.

[97] J. F. Nye. *Physical properties of crystals: their representation by tensors and matrices*. Oxford University Press, 1985.

[98] Y. H. Hu, H. M. Chan, Z. X. Wen, and M. P. Harmer. Scanning electron microscopy and transmission electron microscopy study of ferroelectric domains in doped $BaTiO_3$. *Journal of the American Ceramic Society*, 69(8):594–602, 1986.

[99] J. Hooton and W. Merz. Etch patterns and ferroelectric domains in $BaTiO_3$ single crystals. *Physical Review*, 98(2):409–413, 1955.

[100] L. Jin. Study of ferroelectric domain morphology in PMN-32% PT single crystals. *Ceramics International*, 30(7):1695–1698, 2004.

[101] J. Fousek and M. Safrankova. On the equilibrium domain structure of $BaTiO_3$. *Japanese Journal of Applied Physics*, 4(No. 6):403–408, 1965.

[102] A. K. Tagantsev, L. E. Cross, and J. Fousek. *Domains in Ferroic Crystals and Thin Films*. Springer, January 2010.

[103] S. V. Kalinin, B. J. Rodriguez, S. Jesse, E. Karapetian, B. Mirman, E. A. Eliseev, and A. N. Morozovska. Nanoscale electromechanics of ferroelectric and biological systems: A new dimension in scanning probe microscopy. *Annual Review of Materials Research*, 37(1):189–238, 2007.

[104] L. J. McGilly, A. Schilling, and J. M. Gregg. Domain bundle boundaries in single crystal $BaTiO_3$ lamellae: Searching for naturally forming dipole Flux-Closure/Quadrupole chains. *Nano Letters*, 10(10):4200–4205, 2010.

[105] Y. Cho, S. Kazuta, K. Matsuura, and H. Odagawa. Scanning nonlinear dielectric microscopy with nanometer resolution. *Journal of the European Ceramic Society*, 21(10-11):2131–2134, 2001.

[106] A. L. Roitburd. Equilibrium structure of epitaxial layers. *Physica Status Solidi (a)*, 37(1):329–339, 1976.

[107] A. L. Roytburd, S. P. Alpay, L. A. Bendersky, V. Nagarajan, and R. Ramesh. Three-domain architecture of stress-free epitaxial ferroelectric films. *Journal of Applied Physics*, 89(1):553, 2001.

[108] F. Jona and G. Shirane. *Ferroelectric crystals*. Dover Publications, New York, 1962.

[109] J. Shieh, J. H. Yeh, Y. C. Shu, and J. H. Yen. Operation of multiple 90° switching systems in barium titanate single crystals under electromechanical loading. *Applied Physics Letters*, 91(6):062901, 2007.

[110] R. Hill. Elastic properties of reinforced solids: Some theoretical principles. *Journal of the Mechanics and Physics of Solids*, 11(5):357 – 372, 1963.

[111] A. C. Dent, C. R. Bowen, R. Stevens, M. G. Cain, and M. Stewart. Effective elastic properties for unpoled barium titanate. *Journal of the European Ceramic Society*, 27(13-15):3739–3743, 2007.

[112] J. Kobayashi. Optical observation of domain motion in ferroelectric $BaTiO_3$. *physica status solidi (b)*, 21(1):151–158, 1967.

[113] J. Bornarel. Switching process in ferroelectric-ferroelastic crystals: Velocities of needle shaped domains in KDP. *Ferroelectrics*, 9(1):197–202, 1975.

[114] W. Merz. Domain formation and domain wall motions in ferroelectric $BaTiO_3$ single crystals. *Physical Review*, 95(3):690–698, 1954.

[115] J. X. Zhang and L. Q. Chen. Phase-field model for ferromagnetic shape-memory alloys. *Philosophical Magazine Letters*, 85(10):533–541, 2005.

[116] V. I. Levitas, A. V. Idesman, and D. L. Preston. Microscale simulation of martensitic microstructure evolution. *Physical Review Letters*, 93(10):105701, 2004.

[117] L. J. Li, J. Y. Li, Y. C. Shu, H. Z. Chen, and J. H. Yen. Magnetoelastic domains and magnetic field-induced strains in ferromagnetic shape memory alloys by phase-field simulation. *Applied Physics Letters*, 92(17):172504, 2008.

[118] C. H. Lei, L. J. Li, Y. C. Shu, and J. Y. Li. Austenitemartensite interface in shape memory alloys. *Applied Physics Letters*, 96(14):141910, 2010.

[119] Z. Surowiak, V. M. Mukhortov, and V. P. Dudkevich. Phase transitions and domain structure in heteroepitaxial ferroelectric ($Ba_{1-x}Sr_x$) TiO_3/(100) MgO and $PbTiO_3$/(100) MgO thin films. *Ferroelectrics*, 139(1-4):1, 1993.

[120] N. A. Pertsev, A. G. Zembilgotov, and A. K. Tagantsev. Effect of mechanical boundary conditions on phase diagrams of epitaxial ferroelectric thin films. *Physical Review Letters*, 80(9):1988–1991, 1998.